Memoirs of the Faculty of Science, Kyoto University, Series of Physics, Astrophysics, Geophysics and Chemistry, Vol. XXXVII, No. 2, Article 6, 1988

Measurement of Σ^+ Polarization Parameters in the $\pi^+ + p \to K^+ + \Sigma^+$ Reaction in the Incident Momentum Range between 1490 MeV/c and 2069 MeV/c

By

Junji HABA

Department of Physics, Faculty of Science, Kyoto University, Kyoto 606, Japan

(Received January 19, 1987)

Abstract

Polarization parameters of Σ^+ in the $\pi^+ p \to K^+ + \Sigma^+$ reaction has been measured at 13 momenta between 1490 and 2069 MeV/c in the angular range $-0.1 \leqq \cos\theta^*_K \leqq 0.7$ with higher statistics than previous experiments.

The results are compared with the prediction of the partial wave analysis at Rutherford Appleton Laboratory. Small but significant discrepancies are found. A possible explanation for these discrepancies are discussed.

1. Introduction

Excited states of baryons have been studied experimentally and theoretically for many years. In the early stage of the study, they gave important supports to the theory of quark model and the quantum chromodynamics (QCD). Howerer, the understanding of baryons themselves have not made a great progress, so that it still stands on the phenomenological basis and not on the fundamental theory such as QCD. Our knowledge is far from the comprehensive understanding of many excited states of baryons. The dynamical properties of baryon, such as decay amplitudes, can not be predicted successfully.

Recently several potential models inspired by QCD have been proposed (Ref. 1). Among those, the model due to Isgur, Koniuk and Karl (IKK Ref. 2) has been widely accepted because of its successful and quantitative predictions. The model assumes that at the low q^2, non-perturbative effects of the quark-gluon interaction can be represented by a confining potential, and at the high q^2, the short distant effect can be represented by perturbative corrections due to one gluon exchange. The model is non-relativistic and the spin-orbit effects of the one gluon exchange are arbitrarily neglected. However, in spite of all these assumptions and deficiencies the model gives a remarkably good representation of baryon spectrum.

Not only the mass spectrum but also the hadron properties, which reflect the internal dynamical structures, such as magnetic moments, charge radii etc. must be experimentally studied as extensively as possible so as to progress theoretical understanding of baryons. Various partial decay amplitudes are the most useful among such properties.

Table 1. Summary on the Δ resonances above $K\Sigma$ threshold.

States	Elastic analysis						RAL analysis			other $K\Sigma$ analysis $\sqrt{xx'}$ only		IKK Prediction	
	CMU-LBL			K-H									
Starr rating	mass	width	$\sqrt{xx'}$	mass	width	$\sqrt{xx'}$	Mass MeV	width MeV	$\sqrt{xx'}$	Livanos	Deans	mass MeV	$\sqrt{xx'}$
$S_{31}(1900)$ 3	1890	170	−0.076	1908	140	−0.061			<0.03	—	−0.008		—
$F_{35}(1905)$ 3	1910	400	−0.012	1905	260	−0.023	1960	270	−0.015	−0.013	−0.05	1940 1975	−0.012 −0.001
$P_{31}(1910)$ 4	1910	225	−0.086	1888	280	−0.108			<0.03	−0.019	−0.13	1875 1925	−0.014 −0.072
$P_{33}(1920)$ 3	1920	300	−0.092	1868	220	−0.064	1840	200	−0.052	−0.049	−0.08	1780 1925 1975	−0.051 −0.083 0.0
$D_{35}(1930)$ 4	1940	320	−0.040	1901	195	−0.011			<0.015	−0.031	—		—
$D_{33}(1940)$ 1	1940	200	−0.015		—				<0.015	—	—		—
$F_{37}(1950)$ 4	1950	340	−0.073	1913	224	−0.071	1925	330	−0.053	—	−0.03	1915	−0.043
$S_{31}(2150)$ 1	2150	200	−0.068		—				<0.03	—	—		—
$G_{37}(2200)$ 2	2200	450	−0.016	2215	400	−0.014	2280	400	−0.014	—	—		—
$D_{35}(2350)$ 1	2400	400	−0.114	2305	300	−0.022			0.015	—	—		—
$H_{39}(2300)$ 2	2400	425	−0.019	2217	300	−0.009	2400	200	−0.017	—	—		—
$F_{37}(2400)$ 1	2350	300	−0.035	2425	300	−0.033			<0.015	—	—		—
$G_{39}(2400)$ 1	2300	330	−0.019	2468	480	−0.023			<0.015	—	—		—
$H_{311}(2420)$ 3	2400	450	−0.026	2416	340	−0.026	2400	400	−0.016	—	—		—
Referrence	5)			5)			16)			18)	19)	2)	

$\sqrt{xx'}$ in elastic analysis are SU(3) predicted values.

Recently both the cross sections and polarizations for the $\pi^+ + p \to K^+ + \Sigma^+$ reaction was measured at the Rutherford Appleton Laboratory (RAL) in the momentum range between 1280 MeV/c and 2437 MeV/c using counter techniques (Ref. 3). It provided much more precise and extensive results than the preceding experiments by a bubble chamber (Ref. 4). The partial wave analysis (PWA) on this reaction was also performed at RAL using their data together with the previous one. The results of their PWA are summarized in Table 1 as well as those of other $K\Sigma$ analyses and the prediction from πN elastic analyses (Ref. 5). The predictions of the IKK model above mentioned was also tabulated in the table. The results of the analyses do not exactly agree with each other and also do not always coincide with the prediction of IKK. There are several nice features in this reaction: (a) The intermediate states are the pure I=3/2 states so that the structure of partial waves are much simplified. (b) The inelastic reaction can be described almost in terms of resonances, while the elastic reactions include a large non-resonant (Pomeron exchange) background. Therefore, this reaction is more suitable to observe small effects due to the resonances in spite of the smallness of the cross section.

In the present experiment, the Σ^+ polarization for the $\pi^+ + p \to K^+ + \Sigma^+$ reaction has been measured in the incident momentum range between 1490 and 2069 MeV/c. The present experiment, with counter techniques, has the following salient features: (a) Two charged particles (K^+ and p) in the final state are analysed their momenta with a magnetic spectrometer. (b) Particle species of the charged tracks are positively identified with aerogel Cherenkov counters and time-of-flight (TOF) measurement. (c) With these measured quantities above, the missing mass of K^+ can be calculated to identify the Σ^+. Thus, very pure samples of the Σ^+ production events are selected.

Our apparatus, however, has the limitation in the angular acceptance, because the apparatus is originally designed to measure the asymmetry parameter for the $\Sigma^+\to p\gamma$ decay. The range of the angular acceptance is $-0.25<\cos\theta^*_K<0.85$, where θ^*_K denotes the angle of the K^+ in the CM system.

The direct aims of this experiment are to measure the Σ^+ polarization parameters of the $\pi^+ + p \to K^+ + \Sigma^+$ reaction with four times better statistics than the RAL measurements so as to provide the highly polarized Σ^+'s for the measurement of the asymmetry parameter for the $\Sigma^+\to p+\gamma$ decay. At the same time, the present measurements are also expected to contribute to further partial wave analysis of I=3/2 baryon states.

2. EXPERIMENTAL APPARATUS

2-1 General

The experiment has been performed with a π^+ beam from an intermediate energy beam line (K2) at a 12-GeV proton synchrotron of the National Laboratory for High Energy Physics in Japan (KEK), which is shown in Fig. 1.

Schematic view of our apparatus is shown in Fig. 2. The spectrometer consisted of two almost identical tracking arms, which were placed approximately symmetric with respect to the unscattered beam. Each arm was composed of a trigger scintillation

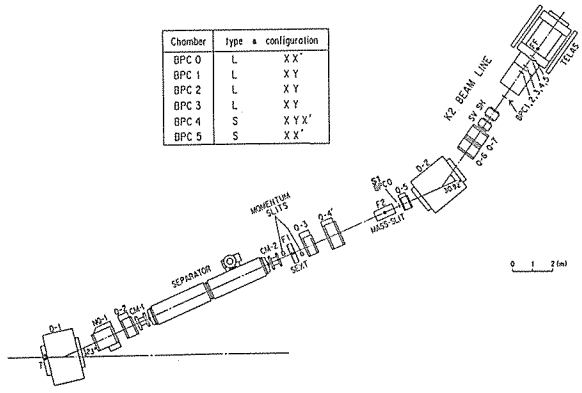

Fig. 1. Schematic view of K2 beam line at KEK PS.

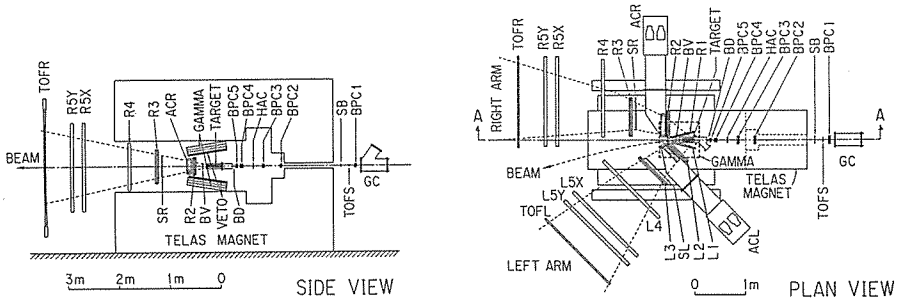

Fig. 2. Layout of the detector system including the spectrometer magnet (TELAS).

counter hodoscope, an aerogel Cherenkov counter, tracking chambers and a TOF scintillation hodoscope.

Two charged particles, the K^+ and proton, in the final state of the $\pi^+ + p \rightarrow K^+ + \Sigma^+$ reaction followed by the $\Sigma^+ \rightarrow p + \pi^0$ decay, were measured their momenta with the tracking chambers in each arm of the magnetic spectrometer. In addition, the K^+ and proton were clearly distinguished with a combination of aerogel Cherenkov counters and TOF counters.

2-2 Beam Line

The K2 beam line was designed to extract well-separated secondary particles in the momentum range from 1.0 GeV/c to 2.0 GeV/c. As is seen in Fig. 1, it consists of two dipole magnets (D1 and D2), three sets of a quadrupole doublets (Q1–Q7), an electrostatic separator (DC separator) with a pair of correction magnets (CM1 and CM2), and finally a pair of steering magnets (SH and SV).

Secondary particles produced from a copper target (50 mm long, 4 mm wide and 5mm high) were focused horizontally at F1 where the momentum of particles were selected with a pair of brass slits. Then the beam was focused vertically at F2 to select the mass of particles by a set of vertical slits with a combination of the DC separator and correction magnets. Finally the beam was focused both horizontally and vertically onto a liquid hydrogen target.

A typical intensity of the primary proton is about 5×10^{11} protons per 400 msec long machine pulse (called "beam spill"), with a repetition rate of one pulse per 2.5 sec. The momentum bites of the secondary beam was chosen by momentum slits to be about $\Delta p/p \sim 1.5\%$. The intensity of the beam was about 7×10^5 per pulse during the experiment and slightly depended upon the momentum of the beam.

2-3 Beam Tagging System

The beam particles were tagged by a set of detectors in the last stage of the K2 beam line. The purposes of this beam tagging system are to reject remaining contaminations in the π^+ beam, to define the beam profile at the trigger level, and to measure precisely the trajectories of beam particles. The locations of these detectors are shown in Fig. 1 and Fig. 2, together with other detectors.

There were five scintillation counters in the beam line; S1, SB, TOFS, BD and HAC. The shapes and sizes of these counters are listed in Table 2. The beam profile at the target entrance was defined practically by a circular counter of BD (30 mm in diameter). The HAC counter which has a 32 mmϕ holes at its center, was used to veto hallo particles. The TOFS counter had a rectangular shape of 100 mm wide, 40 mm high and 5 mm thick and was viewed on the both ends by 2″-photomultiplier tubes (HAMAMATSU R1332). It provided a start timing signal for TOF measurements. The contamination of the K^+ and proton in the incident beam was rejected in the off-line analysis by the TOF measurement between the TOFS and the S1 counter. This TOF measurement is especially useful to the experiment because the K^+p elastic reaction has a large cross section and is difficult to eliminate from the Σ^+ production events due to the same final products.

A gas Cherenkov counter (GC), placed at the down stream of the steering magnets (SV), was employed to reject the contamination of the positrons in the incident beam. The Cherenkov radiator was freon gas at the pressure of 1.6 kg/cm^2, which corresponds to the pion threshold of 2370 MeV/c. Cherenkov lights were detected by a 2″ phototube of HAMAMATSU R1332.

In order to measure precisely the trajectories of the beam particles, six sets of multi-wire propotional chambers (MWPC) (BPC0–BPC5) were installed as is seen in

Table 2. Dimensions of the beam defining counters.

NAME	Size	Characteristic
BD	30ϕ t=3	circular counter
HAC	120×120 t=3	with a 32ϕ hole in the center
SL/SR	540×150 t=5	three of them form a hodoscope which covers the area 540×440
TOF	200×1600 t=30	nine of them form a hodscope which covers the area 1760×1600
TOFS	100×40 t=5	
S1	160×50 t=3	

Fig. 1. These chambers were classified into two types, L and S, in size. The type L had a sensitive area of 144 mm wide and 64 mm high, while the type S was 64 mm wide and 64 mm high. Each chamber set had one or both of the readout planes, X (horizonal coordinate) or Y (vertical coordinate). The chamber structure was the same for both types. Gold plated tungsten wires of 10 μm in diameter were used as anode wires, and were stretched by 10 g tension having 1.0 mm spacing. The half-gap between anode and cathode planes was 4.0 mm. The cathode plane was made of 20 μm thick mylar sheets coated with electric-conductive material of Dotite FC404, whose principal components are carbon graphite (50%) and polyester (50%). With these chamber configurations in conjunction with a gas selection, high and uniform efficiencies were achieved in an intense beam. The details of the readout system and gas selection for these chambers will be described in the section **2-6**.

2-4 Spectrometer Magnet

The spectrometer magnet employed in this experiment was a wide gap C-type magnet. The dimensions of its effective region were 1.5 m long in the beam direction, 1.0 m gap between two pole pieces, and 1.2 m wide. As shown in Fig. 2, the sides and downstream end are widely opened allowing us to install various detectors.

The magnetic fields were measured at the mesh points with 5 cm spacings. The field strength was about 7.0 kG at its center with a nominal supply current of 2000A.

2-5 Liquid Hydrogen Target

The liquid hydrogen (LH_2) target system consisted of three major parts; a LH_2 target container (cell) housed in an outer vacuum vessel, a He refrigerator and a H_2 condenser, and a He compressor. A layout of the system is shown in Fig. 3.

(i) LH_2 target container (called as "appendix")

As shown in Fig. 4, the LH_2 container(cell) was a cylinder of 50 mm in diameter and 300 mm long, and was composed of a 125 μm thick mylar cylinder, hemispherical caps on both ends, and a copper pipe fitting assembly. The caps, made of a 250 μm thick mylar, was fabricated by a "hot drawing method". All the pieces were glued together by a special epoxy regin, of "Armstrong A-4100-E6", which does not

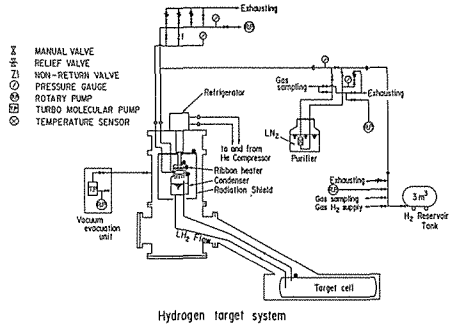

Fig. 3. Schematic diagram of the liquid hydrogen (LH_2) target system.

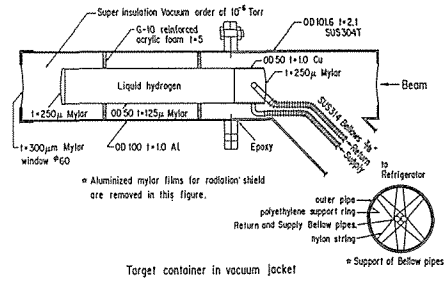

Fig. 4. A close-up view of the target container (cell) and the method to support the bellow tubes.

deteriorate even below 20°K.

The LH_2 container was wrapped with more than ten layers of a thin aluminized mylar film of 12 μm thick to shield thermal radiations (super insulation). Then it was housed in a cylindrical vacuum vessel, which was made of 1 mm thick aluminium to reduce the effects due to the multiple Coulomb scatterings. In order to monitor the level and temperature of liquid hydrogen, several sensors were attached. These included two carbon registers on the top and bottom of the inner surface of the mylar cylinder, and a Pt-thermometric sensor on the bottom of the copper pipe fitting.

(ii) He refrigerator and H_2 condenser

A two stage He refrigerator having a cooling power of about 20W at 20°K was used to liquefy hydrogen.

The H_2 condenser was thermally connected with the second stage of refrigerator. The H_2 condenser was connected to a 3 m^3 H_2 gas reservoir tank through a flexible pipe, and to the LH_2 container through two stainless steel bellow tubes. The bellow tubes were also wraped with more than ten layers of a thin aluminized film for super insulation, as done for the LH_2 container. Each bellow tube was placed inside a vacuum tube, keeping the space between them with nylon strings to avoid thermal contacts. (See Fig. 4.) One of the bellow tube was used as a liquid hydrogen supply line, and the other as a vaporized gas return. In order to increase the thermal conductivity of the supply line, a copper-woven ribbon was soldered to it a thermal anchor.

(iii) Operation

It was found that the purity of He gas was crucial for a stable refrigeration for as long as two weeks. Therefore, He gas was purified with a cold trap of liquid-nitrogen temperature before every cool down operation. At the normal temperature, most of H_2 gas was storaged in the reservoir tank at the pressure of 1.4 kg/cm^2. When the second stage of the refrigerator became about 23°K, H_2 gas started to liquefy in the condenser. Then liquid hydrogen flew to the target container through the supply line. Liquid hydrogen kept evaporating inside the target container until the whole system became ~23°K. It took about 10 hours to fill up the target container with liquid hydrogen. At the stable operation phase, an AC current was applied to a ribbon heater at the condenser to balance with a effective cooling power and keep H_2 gas pressure slightly higer than atmospheric one.

2-6 Tracking Devices

The charged particles were detected in each arm by four sets of MWPC (L1–L4 and R1–R4) and a set of drift chambers (L5 and R5). All of these chamber sets had readout planes for both horizontal (X) and verticla (Y) coordinates, except for L4 and R4 which had only X planes.

(i) Characteristics of MWPC's

Characteristics of MWPC's are summarized in Table 3. All of the chamber planes were read by anode signals except for L1X and R1X planes which were read by cathode induced signals. All of the anode wires were made of gold plated tungsten. The diameter was 20 μm for anode planes with 2 mm spacing for L1, R1, L2Y, R2Y, L3, R3, L4 and R4, and 15 μm with 1.5 mm spacing for L2X and R2X chambers. Cathode

Table 3. Summary of tracking chambers in each arm.

NAME	anode wire diameter	wire spacing	read-out co-ordinate	size (X × Y)	characteristics
L1 /R1	20 μm	2.0 mm	X & Y	400 mm × 288 mm	Y: anode read-out X: cathode read-out
L2X/R2X	20	1.5	X	480 × 320	Al film cathode glued on a honeycomb board
L2Y/R2Y	20	2.0	Y	480 × 320	
L3X/R3X	20	2.0	X	576 × 512	old-fashioned wire cathode
L3X/R3Y	20	2.0	Y	576 × 512	
L4X/R4X	20	2.0	X	1216 × 900	Al film cathode glued on an acrylic foam plate
L5X, Y/ R5X,Y	20	Drift cell 11.5	X or Y	1536 ×1536	Drift chamber with a delay line read-out

planes were made of various materials. These materials were:

L1, R2: a copper strip film laminated with a kapton sheet which was glued on an aramid honeycomb body,

L2, R2: an aluminium film laminated with a kapton sheet which was glued on an aramid honeycomb body,

L3, R3: old-fashioned Cu-Be wire planes, and

L4, R4: an aluminium film laminated with mylar film which was glued on an acrylic foam reinforced with thin G-10 sheet.

In order to measure precisely the X-coordinate of the L1 and R1 chamber planes, signals induced at cathode were amplified and analysed by the standard analog-to-digital converters (ADC). A typical spatial resolution was found to be 150 μm.

(ii) Proportional chamber operating system (LRS PCOS II)

All anode signals from MWPC's were processed by the PCOS system (Ref. 6). The total number of readout channels was about 8000 in this experiment.

In order to check whether complicated serial data were transferred successfully to the encoder, a fixed hit pattern was generated and was monitored during the entire course of the experiment. If this test pattern was not recorded correctly on data tapes, corresponding event was excluded from off-line analysis.

(iii) Gas used for MWPC's

Two types of MWPC's gas were employed in this experiment. Both of the two types were modified versions of the so called "magic gas" (Ref. 7). The contents of

Table 4. List of gas mixture used in tracking chambers.

Type I		Type II		Drift chamber	
Ar	69.1%	Ar	70.3%	Ar	50.0%
Isobutane	23.2%	Isobutane	14.2%	Ethane	50.0%
Freon	0.4%	Freon	0.6%		
Methylal	7.3%	Methylal	14.9%		

these gases are listed in Table 4. The type-I gas, which contained more quencher and freons in it, was suitable to operate in the high counting condition. However, it is not adquate for chambers with 2 mm anode wire spacing because of the low efficiency. This type-I gas was used for all beam chambers (BPC0-BPC5), and L2X and R2X. The type-II gas was used for all other MWPC's.

(iv) Drift chambers

Characteristics of the drift chambers are listed in Table 3. Each drift chamber plane had the same cell structure; they were made of a plane with potential and sense wires altermating each other, sandwiched between two cathode planes. In order to resolve left-right ambiguities, a single drift cell had a pair of sense wires with 1mm spacing. The maximum drift length was then 11.5 mm.

Eight consecutive sense wires were grouped together and all of their ends on one side were connected serially with coaxial delay lines to reduce the number of electronic channels. Then this delay chain was read on both ends to measure timing. Signals were amplified and discriminated by monolithic IC's (LRS MVL100 Ref. 6). Then the timing was digitized by the standard time-to-digital converters (TDC). In the off-line analysis, the drift time in a cell and the hit wire address in a group were evaluated by taking a sum and a difference in pair of timing information, respectively. The gas used for the drift chambers was argon-ethane mixture (50%–50%).

2–7 Aerogel Cherenkov Counters

Silica aerogel Cherenkov counters(ACL or ACR) were employed to reduce triggers from the background of π^+ inclusive reactions. The aerogel radiator had a refractive index of 1.06, which corresponds to the threshold of 400 MeV/c for pions. The counters were placed behind L2/R2 in both tracking arms. Each counter consisted of an aerogel radiator block (40 cm wide, 30 cm high and 9cm thick constructed with 18 pieces of 20 $\times$10$\times$3 cm), a light guide of air duct with inner surfaces covered with aluminized mylar sheets, and four 5″-photomultiplier tubes placed in an iron box to shield them from a strong leakage flux of the spectrometer magnet. Fig. 5 shows a schematic view of the counters. The constant flow of dry nitrogen was kept during the experiment to protect the radiator being spoiled by humidity in the air. The gain and threshold level of the counters were monitored every two weeks throughout the experiment.

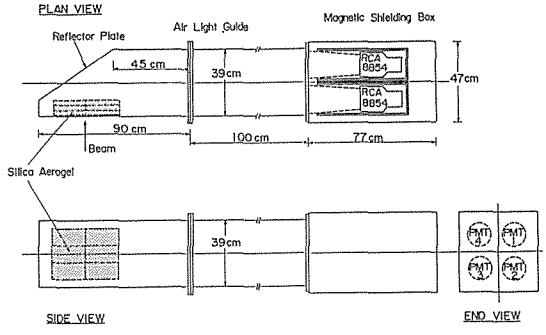

Fig. 5. Schematic view of the aerogel Cherenkov counter.

The photomultilpier tubes (RCA8854) called "quantacon" were used for these counters, and they had a very high gain at the first dynode due to the special material employed (GaAsP). As a result, they could discriminate even a single photoelectron from noise, and could count very weak Cherenkov lights reliably. By using 1 GeV/c pion beam, the average photoelectrons was found to be five in all effective region, and the detection efficiency of 99.3% was expected from the calculation of photon statistics based on the Poisson distributions. The datailed description on the counters can be found in Ref. 8. The multiple Coulomb scattering in the aerogel radiator (~0.1 radiation length) degraded the momentum resolution and vertex resolution substantially.

2-8 Time-of-flight Hodoscope

The TOF scintillation hodoscope (TOFL or TOFR) was placed at the end of each tracking arm to determine which arm tagged K or proton. Each hodoscope was composed of nine identical scintillation counters (20 cm wide, 160 cm high and 3 cm thick) which were viewed by two 2″-photomultiplier tubes on both ends. Each counter was placed overlapping with adjacent counters by about 5mm. The total effective area of each hodoscope was 176 cm wide and 160 cm high.

The start timing for the TOF measurements was provided by the TOFS counters placed at the entrance of TELAS magnet.

Several cares were taken to improve the timing resolution. These are: (a) the usage of photmultiplier tubes (HAMAMATSU R1332) of "quantacon" type in conjunction with the application of high enough voltage between the cathode and first dynode, (b) the correction for time jitters due to the pulse heights, and (c) the careful design of light guide and scintillator wrapping etc. Details are described in Ref. 9. The time resolution was about 200 psec during the entire period of the experiment.

2-9 Fast Electronics

A schematic diagram of our fast trigger logics is shown in Fig. 6. They were constructed as follows.

(a) The beam particle entering into the LH_2 target were defined as

$$BEAM = SB * TOFS * BD * \overline{HAC} * \overline{GC},$$

where SB etc. represent the discriminated signals of the corresponding counters.

(b) Next, the reactions of incident particles were defined by being vetoed with the $BV1$ and/or $BV2$ counters (beam veto counters as seen in Fig. 2) as

$$REACT = BEAM * \overline{BV1 + BV2}.$$

(c) The charged particles in the tracking arms were then defined by

$$LEFT = SL * TOFL * \overline{ACL},$$
$$RIGHT = SR * TOFR * \overline{ACR}.$$

The logic signals $SL(SR)$ and $ACL(ACR)$ were generated when at least one photomultilplier tube had a signal larger than a preset value. On the other hand, the

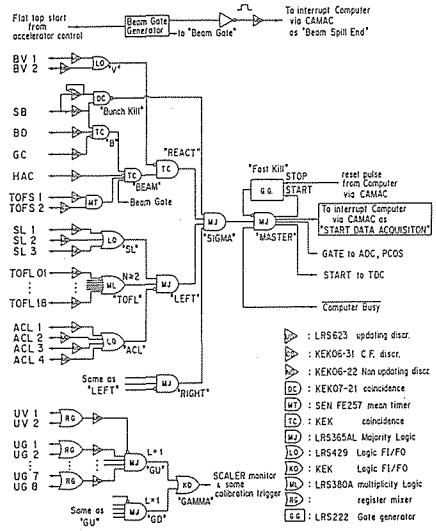

Fig. 6. Logic diagram of fast electronics.

logic signal *TOFL*(*TOFR*) required signals from at least two photomultiplier tube signals, because each counter was viewed by two photomultiplier tubes on both ends.

(b) Then the master trigger was generated from the combination of above all logics as follows;

$$SIGMA = REACT * LEFT * RIGHT * \overline{Bunch\text{-}Kill}\,,$$
$$MASTER = SIGMA * \overline{computer\ BUSY} * \overline{FAST\text{-}Kill}\,.$$

The signal *Bunch-Kill* was generated whenever two successive beam particles arrived within 20 nsec. The actual circuit consisted of two types of discriminators, updating and non-updating (See Ref. 10). It is obvious that the logic signal *SIGMA* essentially represented the occurrence of the reactions and the existence of two or more charged particles (but not pions with $p>400$ MeV/c) in both arms.

The *MASTER* signal was then formed from *SIGMA* and two other minor gate signals; the computer *BUSY* signal was generated by the on-line computer PDP11/45 and *FAST-Kill* was a kind of S/R type flip flop which would be set by *MASTER* itself and be reset after the data acquisition by the computer via an CAMAC output register.

Upon the occurrence of *MASTER*, it would open the gate for ADC's, PCOS for MWPC's and Coincidence registers, and start TDC's and an encoding of PCOS. After about 1 msec, the on-line computer was interrupted and requested to read all data via the CAMAC system.

2-10 Date Acquisition

The on-line computer system was a complex of a CAMAC, PDP11/45 and KEKX system. KEKX is a name of the system composed of an intelligent CAMAC interface called "CCS-11" whose CPU is equivalent to PDP11/23, and its software for the data acquisition and data analysis/monitoring, which is working under RSX11-M. Details

of KEKX can be found in Ref. 11.

The following information from the detectors were transferred to the computer and written onto magnetic tapes.

i) Pulse heights of all TOF counters digitized by ADC's(LRS 2249A).
ii) Pulse timings of all TOF's and S1 counters analysed by TDC's(LRS 2228A).
iii) Pulse heights of all aerogel Cherenkov counters digitized by ADC's(LRS 2249W).
iv) Encoded hit patterns of MWPC's in PCOS encoders(LRS 2700).
v) Timing of pulse from drift chambers L5 and R5 analysed by TDC's(LRS 2228).
vi) Hit patterns of all scintillation counters with coincidence registers.
vii) Number of counts recorded in various scalers.

All data were collected for every *MASTER* trigger except vii), and were buffered in the CCS-11 memory and transferred to the magnetic tape at the end of every beam spill. The data vii) was read and also recorded on the magnetic tape only at the spill end.

During the experiment, the detector status with several histograms of ADC or TDC, chamber hit distribution, and failure rate of PCOS encoding process were displayed by the on-line system. Various types of graphical display for each event were also available.

The power supply voltages for photomultiplier tubes, various chambers, the DC separators, etc. .were also monitored by a personal computer (NEC PC9801).

3. DATA REDUCTION AND ANALYSIS

Data were collected at 13 incident momenta of 1490, 1548, 1598, 1649, 1705, 1748, 1803, 1845, 1895, 1939, 1986, 2027 and 2069 MeV/c. The averaged number of triggered events was about 17×10^4 with the π^+ beam flux of 2×10^9 at each momentum except at p_{in}=1705 MeV/c. As was mentioned, at p_{in}=1705 MeV/c the $\Sigma^+\to p\gamma$ decay experiment was performed, so that about 6×10^7 trigger events were collected. In this analysis 17×10^5 trigger events were used at this momentum.

3-1 General

The data in the raw magnetic tapes (MT) were processed with the KEK central computer (HITAC) system. The data reduction processes were divided into several steps called as "phase". In the first phase, the raw MT's written by the on-line computer were converted to HITAC standard tapes. No event selection was made in this phase. In the second phase, a quick (but somwhat crude) event reconstruction was performed to select only those events that had the mass of scattered particles in both arms greater than 300 MeV/c^2. Then, in the third phase, all necessary kinematical variales and informations of trajectories were calculated as precisely as possible. In the fourth phase, various software cuts were applied to select the events of the $\pi^+ + p\to K^+ + \Sigma^+$ reaction. This event sample was used to calculate the Σ^+ polarization (see §4-1).

3-2 Data Reduction I

In the second phase, momenta of charged particles were calculated from their

trajectories on track chambers in both arms. The quintic spline method due to Wind (Ref. 13) was employed to reconstruct the trajectories. The tracks were required to have hits on at least five out of nine chamber planes and to have single hit on those chamber planes. For each event, it was required to have one reconstructed track in each arm of left and right, beacuse the $\pi^+ + p \to K^+ + \Sigma^+$ reaction was expected to yield two charged particles. The efficiency of reconstruction in both arms was estimated to be about 75%.

Then particle's velocity, $v=\beta c$, was calculated from the time of flight measured by the TOF system and path length of flight determined in the track reconstruction procedure. The particle mass m was given by

$$m = \frac{p}{\gamma\beta}: \qquad \gamma^2 = (1-\beta^2)^{-1}, \tag{1}$$

where p represents the momentum of particle. A two dimensional plot of momentum versus mass squared for the detected particle is displayed in Fig. 7. Three clusters corresponding to the π^+, K^+ and proton are clearly seen At this point, the events were required to have two charged particles with the mass greater than 300 MeV/c^2 to reduce the background from π^+ inclusive reactions. Finally those selected enents were written onto the data summary tapes (DST2) with all informations calculated in this phase together with the raw data further analysis.

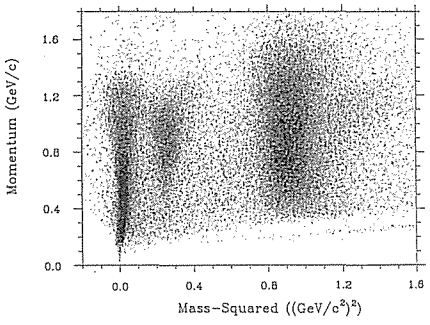

Fig. 7. Two dimensional plot of momentum versus mass squared determined by TOF. Three clusters corespond to π^+, K^+ and proton are clearly seen in this plot.

The third phase is to reconstruct precise trajectories by the Runge-Kutta method. (See Appendix-A). The advantages of this method over the spline reconstruction procedure are the following: (a) For the given vertex point and momentum vector of the particle, it solves and integrates the exact equation of motion by referring the magnetic field. Therefore, by choosing an integration step small enough, it is possible to calculate a trajectory with a better precision. (b) This method can take into account the multiple scattering and energy loss in various materials such as chamber walls, scintillators and aerogel radiator etc. In the actual procedure, the best vertex point and three momentum vector were found by minimizing χ^2 values defined by the differences between the measured and expected chamber hit positions. The minimization of χ^2 was controlled by the program "MINSQ" developed at CERN, which was based on the Powell method (Ref. 13). The detailed description of the track reconstruction procedure can be found in Appendix-A.

The next step in this phase was to determine trajectories of incoming beam particles. The same method above mentioned was applied to the every hit position of the beam chambers, too.

Then the vertex of Σ^+ production in the $\pi^+ + p \rightarrow K^+ + \Sigma^+$ reaction and the vertex of the $\Sigma^+ \rightarrow p + \pi^0$ decay were determined. In the present analysis, these vertices were defined as follows. For each event, the track with lighter mass was assigned "K" and the other as "p". The vertex of Σ^+ production was defined as the mid point of the segment where the distance between the "K" assigned track and the beam track was minimum. The vertex of Σ^+ decay was also defined as the mid point of the segment where the distance between the "p" assigned track and "Σ" track was minimum. Here the "Σ" track was calculated from the "K" momentum and beam momentum with the aid of the reaction kinematics. A typical Z-distribution (the projected position onto the beam direction) of the vertex of Σ^+ production was shown in Fig. 8, where the profile of the LH_2 target and the trigger counter (BD) can be seen.

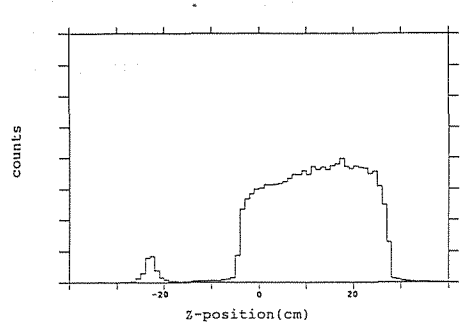

Fig. 8. Distribution of Σ^+ production vertex (defined in § 3-3). The profile of the taget container is clearly seen in the region $-5\,\text{cm} < z < 25\,\text{cm}$. The counter BD is identified as the small peak near the point $z = -20$ cm. The beam particles passed from left side to right.

Finally, by using these vertices and trajectories, the flight length of the particle was calculated again in order to determine the precise particle's mass.

The third phase ended by writting the raw events data onto the DST3 tapes together with all kinematical variables determined in this phase.

3-3 Data Reduction II

The $\pi^+ + p \rightarrow K^+ + \Sigma^+$ events were further selected by starting from the DST3 tapes which contain roughly selected events with all necessary kinematical variales. The following software cuts were applied.

(a) In order to reject the K^+ or proton contamination in the incident beam, a cut was applied to the spectrum of TOF between S1 and TOFS counters. The actual position of theis cut was dependent upon the incident momentum.

(b) The fiducial cut was applied on the effective area of L3 or R3 determined by the Monte-Carlo simulation.

(c) The confidence level obtained in the track reconstruction procedure in the third phase was required to be larger than 10^{-4}. Simultaneously, a number of chamber planes with only one hit were required to be greater than six. This cut rejected the fake evnets with spurious hits.

(d) The vertex of Σ^+ production was required to be inside the fiducial volume of the

LH_2 target, where the radial position was less than 60 mmϕ and the Z-position was in the region of $-50<z<250$ mm.

(e) The decay vertex was required to lie in the region between the target and the L1 or R1 chamber.

(f) The cuts of mass determined by TOF for the outgoing particles assigned as "K" (see § 3-2 for the assignments) were 350 MeV/$c^2<m<750$ MeV/c^2 while those as "p" were 800 MeV/$c^2<m<1050$ MeV/c^2.

(g) The minimal distance between the Σ^+ and proton tracks had to be less than 8 mm.

The event samples survived at this step were mostly composed of the $\pi^++p\to K^++\Sigma^+$ reaction. To demonstrate this, the missing mass M_X given by the following equation was calculated.

$$M_X^2=(E_{in}+m_p-E_K)^2-(p_{in}-p_K)^2\,, \tag{2}$$

where, m_p is the proton mass (938 MeV/c^2), E_K and p_K denote the energy and momentum of the particle assigned as "K", respectively. A typical distribution of M_X (for $p_{in}=1705$ is shown in Fig. 9 as a solid line, where a clear peak of Σ^+ can be seen with a small and broad peak of Σ^*(1385). A flat background beneath the peaks comes mainly from pion production reactions.

(h) In order to reduce this background, the mass of the missing neutrals in the $\Sigma^+\to p+\pi^0$ decay was calculated and is shown in Fig. 10. This distribution well coincides with that of π^0 and the arrows indicate the cut position applied here. After the cut, the missing mass distribution of Σ^+ became cleaner than the previous one as shown by a dashed curve in Fig. 9.

(i) The final cut was applied to the mass distribution, which is 1150 MeV/c^2 $<M_\Sigma<$1250 MeV/c^2, the background in the final samples was estimated to be less than

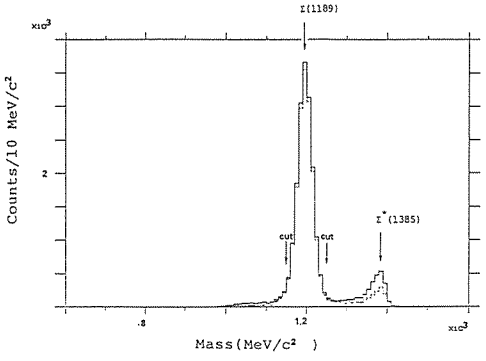

Fig. 9. Missing mass distribution of Σ^+. The solid curve indicates the distribution before the application of π^0 mass cut indicated by a solid curve. The dominant peak at 1189 MeV/c corresponds to the Σ^+ particles. Σ^+(1385) is also seen. The dashed curve indicates the missing mass distibution of the final sample. Arrows indicate the position of cut.

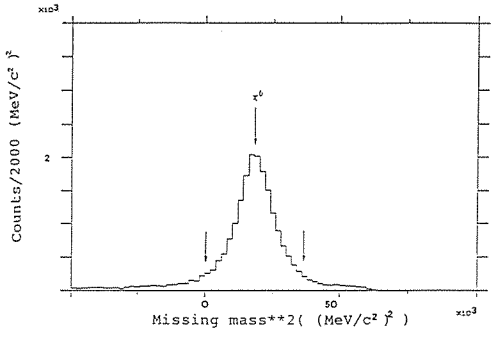

Fig. 10. Missing mass squared of π^0. Arrows indicate the position of cut.

0.5%.

Typical surviving rates for individual software cuts are listed in Table 5. The numbers of the final event samples for each incident momentum obtained in this way are summarized in Table 6.

Table 5. Summary of cuts applied on the event in DST3 and typical numbers of surviving events at p_{in}=1705 MeV/c.

Soft ware cuts		NO. of survivals (Total No. (K left, K right))
TOF of beam particle	a)	81785
Fiducial cut	b)	58251
χ^2 of track fitting	c)	49415(24167, 25248)
Σ^+ produced in LH_2 and decay in L1/R1 region	d,e)	44193(21582, 22611)
Fine cut on arm TOF ($\pi/K/p$ selection)	f)	39088
π° mass cut	h)	33513(16017, 17496)
Σ^+ mass cut	i)	29764(14132, 15632)

Table 6. Summary of Number of final samples. "K in left (right)" means that the K^+ was tagged in left (right) arm.

P_{lab}	E_{cm}	K^+ in Left	K^+ in Right	Total
1490	1926	1267	1795	3062
1548	1954	1541	2012	3553
1598	1977	1450	1746	3196
1649	2001	1406	1681	3087
1705	2027	14132	15632	29764
1748	2047	1910	1998	3908
1803	2072	1490	1435	2925
1845	2091	1324	1293	2617
1895	2113	1554	1420	2974
1939	2133	1014	1003	2017
1986	2153	1283	1249	2532
2027	2171	987	1039	2028
2069	2189	1273	1245	2518
(MeV/c)	(MeV)			

3-4 Determination of the Incident Beam Momentum

The incident momentum is determined by analysing the event of the proton-proton elastic scattering, which are contained in the DST2 tapes. Because of the imperfection of the mass selection by the DC mass separtor in the K2 beam line, a small amount of protons were contained in the incident beam. The events from the proton-proton elastic scattering were selected as follows.

(a) The TOF information over the scintillation counter S1 and TOFS was used to select protons in the incident beam. Fig. 11 shows the TOF spectrum at p_{in}=1705 Mev/c as an example. A cut was applied at the TDC counts of 480. (Hereafter in this section, figures are shown at p_{in}=1705 MeV/c as examples).

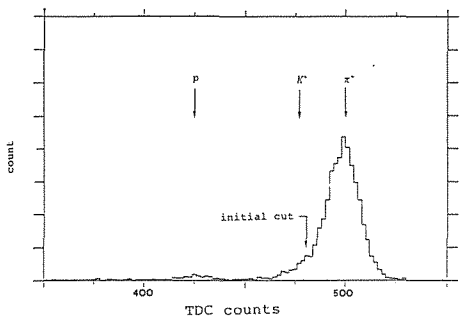

Fig. 11. TOF between S1 and TOFS counters for the incident beam particles. A dominant peak around 500 TDC count corresponds to π^+. The K^+ and protons are barely seen.

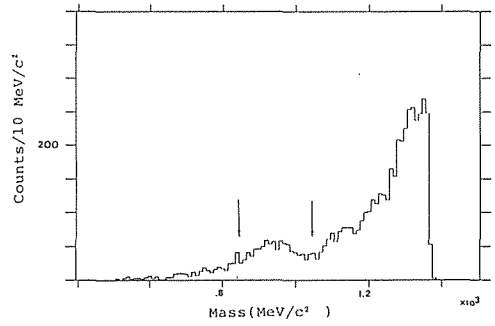

Fig. 12. Missing mass plot M_R. The peak corresponding to proton is seen around 900 MeV/c^2. Arrows indicate the position of cut.

(b) The particle mass in each tracking arm was calculated in the same way as described in the section 3-2. The particle having the mass m within the range of 800 MeV/c^2<m<1050 MeV/c^2 were defined as "protons", and selected.

(c) The missing mass M_R was calculated for thus selected events according to the formula

$$M_R^2=(E_{in}+m_p-E_L)^2-(p_{in}-p_L)^2\,, \tag{3}$$

where E_{in} and p_{in} are nominal values of the incident energy and momentum, respectively. E_L and p_L represent the energy and momentum of the particle in left arm assuming the proton mass, respectively. Fig. 12 shows the missing mass distribution, in which the proton peak is barely seen. Only those events with 840 MeV/c^2<M_R<1040 MeV/c^2 were selected for the following step.

(d) The missing mass M_L was also calculated by replacing E_L and p_L in the equation (3) with E_R and p_R determined by the right arm. The spectrum is shown in Fig. 13 in which the proton peak is clearly seen. The same mass cut was also applied on M_L.

(e) The TOF distribution for these events shows a clean peak corresponding to the protons as is seen in Fig. 14. A final cut was applied as indicated in this figure by the arrows.

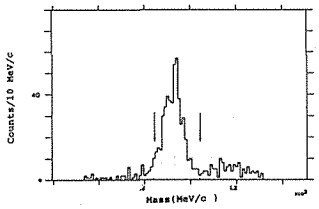

Fig. 13. Missing mass plot M_L. The peak corresponding to proton is seen around 900 MeV/c^2. Arrows indicate the position of cut.

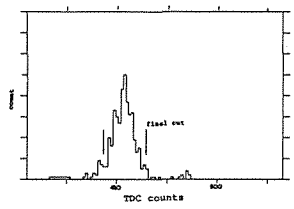

Fig. 14. TOF distribution of the incident beam particles for the events finally selected as the pp elastic reaction. The peak corresponding to proton is clearly seen.

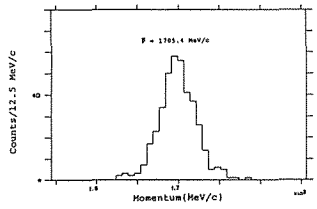

Fig. 15. Momentum sum of P_L and P_R. The momentum is determined as 1705 MeV/c by averaging this distribution.

(f) Finally the momenta p_L and p_R were summed up to evaluate the incident momentum. Fig. 15 shows such a spectrum, from which the average beam momentum was evaluated.

The average momentum thus obtained is adopted as the incident momentum p_{in}.

4. RESULTS AND DISCUSSIONS

4-1 Polarization

The angular distribution of emitted protons from the $\Sigma^+ \to p + \pi^0$ decay in the Σ^+ rest frame is give by

$$\frac{1}{N_0}\frac{dN}{d\cos\theta_p} = \frac{1}{2}(1+\alpha_0 P_\Sigma \cos\theta_p), \tag{4}$$

where P_Σ denotes the polarization parameter of the Σ^+ production to be measured, α_0 is the decay asymmetry parameter and θ_p is the angle between the direction of emitted proton and the normal to the Σ^+ production plane. The value of α_0 has been measured by many experiments, and is -0.980 ± 0.015 on an average (Ref. 14). P_Σ depends upon both the incident π^+ momentum and the scattering angle θ^*_K which is defined as the angle between the incident π^+ and the outgoing K^+ in the CM frame. Therefore, the final event samples, obtained in the previous section, were divided into the $\cos\theta^*_K$ bins at each incident beam momentum p_{in}. The width of the $\cos\theta^*_K$ bin was chosen to be 0.1 which is larger than our angular resolution.

The final event samples were further subdivided into the $\cos\theta_p$ bins. A Monte Carlo simulation was performed to evaluate the acceptance of our apparatus as a function of $\cos\theta_p$ at each incident momentum p_{in} and $\cos\theta^*_K$. Approximately ten times more events than measured events were calculated to reduce the statistical uncertainty

of the simulation to be negligible. Finally the $\cos\theta_p$ distribution corrected with the acceptance were fitted to the equation (4) to find $\alpha_0 P_\Sigma$. An example of the $\cos\theta_p$ distribution at $p_{in}=1705$ MeV/c and at $\cos\theta_K^*=0.1\pm0.05$ is shown in Fig. 16, where the solid line represents the straight line of $1+\alpha_0 P_\Sigma\cos\theta_p$ obtained by the fit. The polarization $\alpha_0 P_\Sigma$ thus obtained for each $\cos\theta_K^*$ bin at all incident momenta were plotted in Fig. 17 and were tabulated in Table 7. The errors include both the statistical uncertainties

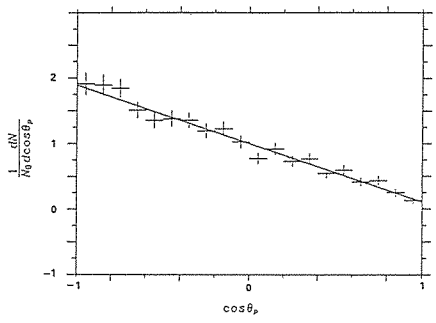

Fig. 16. Typical $\cos\theta_P$ distribution corrected with the acceptance at $0.05<\cos\theta_K^*<0.15$, and at $p_{in}=1705$ MeV/c. + represents the results and a solid line represents a fit to the equation (4).

Table 7. Measured polarization parameters $\alpha_0 P_\Sigma$ in the present experiment. The systematic errors (<5%) are not included in the error listed here. P_{lab}: the momentum of the incident π^+, E_{cm}: the total energy in the CM frame.

$P_{\rm lab}$	$E_{\rm cm}$		$\cos\theta_{\rm k}^*$ −0.1	0.0	0.1	0.2	0.3	0.4	0.5	0.6	0.7
1490	1926		+0.23	−0.19	−0.36	−0.63	−0.67	−0.67	−0.83	−0.93	+0.07
		±	0.13	0.13	0.10	0.11	0.09	0.12	0.13	0.20	0.23
1548	1954		−0.28	−0.38	−0.75	−0.92	−0.79	−0.82	−0.91	−0.93	−0.78
		±	0.14	0.12	0.08	0.07	0.09	0.08	0.10	0.13	0.19
1598	1977		−0.33	−0.62	−0.61	−0.81	−0.96	−1.01	−1.03	−1.00	−0.69
		±	0.11	0.10	0.09	0.07	0.06	0.08	0.08	0.12	0.21
1649	2001		−0.35	−0.61	−0.73	−0.90	−1.05	−0.88	−0.93	−1.17	−0.86
		±	0.18	0.12	0.09	0.08	0.07	0.07	0.08	0.10	0.22
1705	2027		−0.12	−0.58	−0.85	−0.92	−0.95	−0.93	−0.91	−0.88	−0.74
		±	0.05	0.03	0.02	0.02	0.02	0.02	0.02	0.02	0.06
1748	2047		−0.37	−0.71	−0.95	−1.10	−0.98	−0.97	−1.02	−0.89	−0.67
		±	0.18	0.10	0.07	0.07	0.05	0.05	0.05	0.09	0.19
1803	2072		−0.45	−0.57	−0.94	−1.08	−1.04	−0.94	−0.96	−0.81	−0.63
		±	0.24	0.14	0.10	0.06	0.05	0.06	0.08	0.12	0.26
1845	2091		−0.10	−0.95	−0.86	−0.85	−0.91	−0.85	−0.88	−0.91	−0.53
		±	0.23	0.12	0.08	0.08	0.07	0.07	0.09	0.11	0.29
1895	2113		−0.18	−0.85	−0.98	−0.92	−0.97	−0.76	−0.99	−0.82	−0.75
		±	0.25	0.12	0.11	0.07	0.06	0.07	0.07	0.09	0.25
1939	2133		−1.01	−0.57	−1.07	−1.02	−0.86	−0.86	−1.00	−0.96	−0.74
		±	0.40	0.20	0.12	0.07	0.09	0.08	0.08	0.12	0.35
1986	2153		−0.35	−0.95	−1.05	−0.91	−0.79	−0.91	−0.61	−0.83	−0.71
		±	0.32	0.15	0.10	0.07	0.07	0.07	0.09	0.12	0.26
2027	2171		−0.88	−0.96	−0.97	−1.08	−0.85	−0.88	−0.86	−0.82	−0.53
		±	0.40	0.21	0.10	0.08	0.08	0.08	0.10	0.14	0.37
2069 (MeV/c)	2189 (Mev)		−0.42	−0.86	−1.15	−0.85	−0.64	−0.67	−0.53	−0.76	−1.03
		±	0.27	0.17	0.09	0.08	0.08	0.08	0.10	0.10	0.28

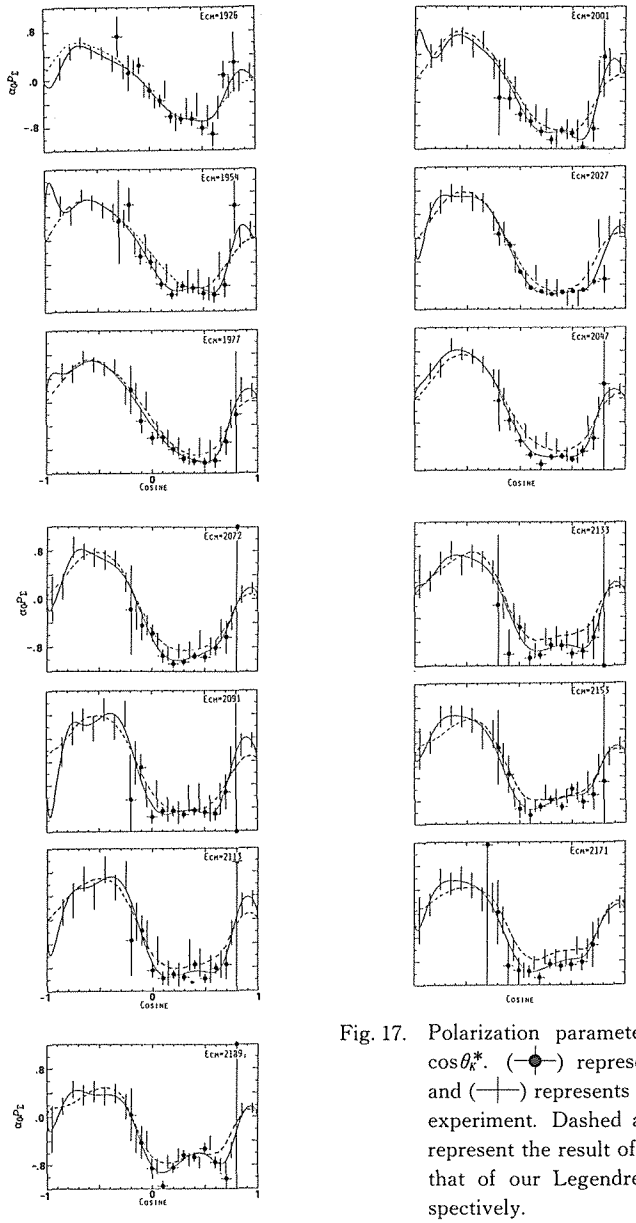

Fig. 17. Polarization parameters $\alpha_0 P_\Sigma$ versus $\cos\theta_K^*$. (—●—) represents our results and (—┼—) represents that of the RAL experiment. Dashed and solid curves represent the result of RAL PWA and that of our Legendre expansion, respectively.

and the goodness of the fits. In Fig. 17, the experimental results at the RAL are also shown by daggers (Ref. 3).

4-2 Consistency Checks and the Systematic Errors

In order to demonstrate the reliability of the data reduction, various consistency checks were applied to the results.

Fig. 18 shows the proper decay length of the Σ^+, which is defined as the distance between the production and decay vertices divided by a Lorentz factror. The distribu-

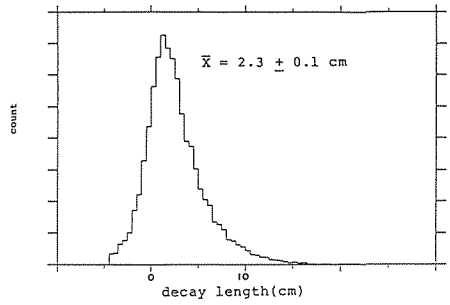

Fig. 18. Distribution of the proper decay length. The mean of this distribution, which is equal to the slope of decay exponential, is 2.3 ± 0.1 cm and is consistent with the Σ decay length $l_0=2.4$ cm.

tion of proper decay length must follow the exponential curve convoluted with the spatial resolutions of decay vertex. The mean value of the proper decay length was found to be 2.3 ±0.1 cm and agrees well with $l_0=2.4$ cm quoted for the Σ^+ by PDG (Ref. 14).

As mentioned above, the $\cos\theta_p$ distribution should follow a straight line represented by the equation (4). But there are many potential sources which would distort the distributions. The average value of χ^2 was found to be about $1.1\times N_{DF}$, where N_{DF} denotes the degree of freedom and is 18 in this case. Therefore, the statistical uncertainty is scaled up by a factor of 1.1 to include some systematic errors due to unknown local inefficiencies in the detectors.

The present detector system was placed roughly symmetric with respect to the unscattered beam in the horizontal plane, and then the final event samples can be divided into the two subsets; one in which the K^+ were tagged in the left arm ($\theta_K^*>0$) and the other in the right arm ($\theta_K^*<0$). The spin directions of the Σ for the same $\cos\theta_K^*$ were opposite each other for these two subsets of data. Therefore, any asymmetries in the detector system would result in a non-zero value of the difference between the polarization $\Delta P=P_L-P_R$.

The difference ΔP was used to estimate the possible systematic errors by the following two methods.

(a) $\Delta P=P_L-P_R$ for each data points of $\cos\theta_K^*$ bins at 1705 MeV/c was calculated and is plotted with its error of $\sqrt{\Delta P_L^2+\Delta P_R^2}$ in Fig. 19. The weighted mean of ΔP was found to be only -0.01.

(b) The normalized polarization differences defined as

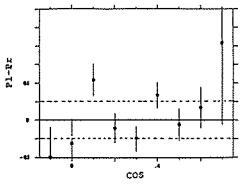

Fig. 19. $\Delta P=P_L-P_R$ at $p_{in}=1705$ MeV/c as a function of $\cos\theta_K^*$. The systematical error(<5%) are indicated with two doted lines.

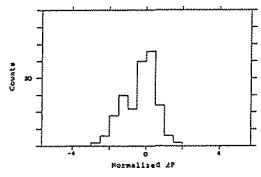

Fig. 20. Distribution of the normalized polarization difference ($\Delta\tilde{P}$) for all data except for those at 1705 MeV/c.

$$\Delta\tilde{P} = (P_L - P_R)/\sqrt{\Delta P_L^2 + \Delta P_R^2}$$

where calculated for each (nine) $\cos\theta_K^*$ bins at 12 momenta except for p_{in}=1705 MeV/c (108 points in total). If there are no systematic errors, the quantity $\Delta\tilde{P}$ must normally distribute with unit standard deviation around zero. Fig. 20 shows such a distribution. The resultant rms deviation is close to 1, but the meam value was found to be -0.34. This value is significantly large in the view of statistics, because the uncertainty on it is expected $1/\sqrt{N_{\text{points}}}$, and is about 0.1. The systematic error (ΔP_{sys}) in terms of the polarization was condidered to be $-0.34\times\langle\Delta P_{\text{stat}}\rangle$, where ΔP_{stat} is an average statistical uncertainty ($\sim$0.13). Finally the systematic error was estimated to be 5%. This value can explain the deviation of ΔP at 1705 MeV/c as is seen in Fig. 19.

It should be stressed here that the final polarization presented in Fig. 17 and Table 7 are the averaged values of both P_L and P_R. Therefore, false polarizations due to the asymmetries of the detector would at least partially, cancel each other.

4-3 Comparison with the RAL Results

By comparing the present results with the experimental results at the RAL, the following points are worth noticing.

(a) In general, both experimental results agree well with each other within statistical errors.

(b) Crudely speaking, our statistical errors are a half of the RAL, although our angular range is limited.

(c) With a close examination, our data shows slightly but systematically larger negative polarizations than the results at RAL.

(d) In particular, our results have wide and flat shapes in the region of $\cos\theta_K^*>0$ at several momenta. This feature suggests that the contribution from higher waves must be carefully examined.

4-4 Legendre Polynomial Expansion

In general, the differential cross section and polarized cross section may expanded in terms of Legendre polynomials as

$$\frac{d\sigma}{d\Omega} = \frac{1}{q^2}\sum_{k=0}^{n} A_k P_k(\cos\theta), \tag{5}$$

$$P\frac{d\sigma}{d\Omega} = \frac{1}{q^2}\sum_{k=1}^{m} B_k P_k(\cos\theta), \tag{6}$$

where $P_k(P_k^1)$ is the Legendre (1st associated Legendre) polynomial and q^2 denotes the beam momentum squared in the CM frame in units of cm^{-2}. (ie. inverse square of wave length) The coefficients A_k and B_k can be expressed as binominal expansions of the partial waves in the formation channel and hence they contains information on the resonances. (See Ref. 10 and 15.)

In the present experiment, such independent expansion is not possible because only polarizations have been measured in the limited angular range. Therefore, the differential cross sections needed in the equation (6) were substituted with the cross section

calculated from the results of the RAL partial wave analysis (PWA) (Ref. 16). For the polarizations, both the present results and the RAL results were used, expecting main features would be controlled by the present results due to the small statistical errors. In this way, it is expected to extract the essential features of the present results.

The actual expansions were performed with the aid of the program "MINSQ" which was already used in the track fitting procedures. First of all, the order of expansion required for the equations (5) and (6) was determined. The confidence level

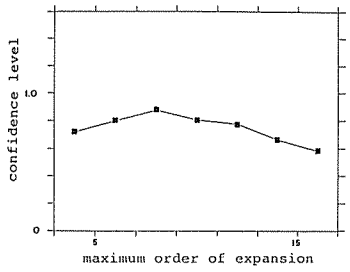

Fig. 21. Confidence level of the Legendre expansion as a function of the maximum order used in the expansion. In the present analysis, the expansion up to N=10 was made.

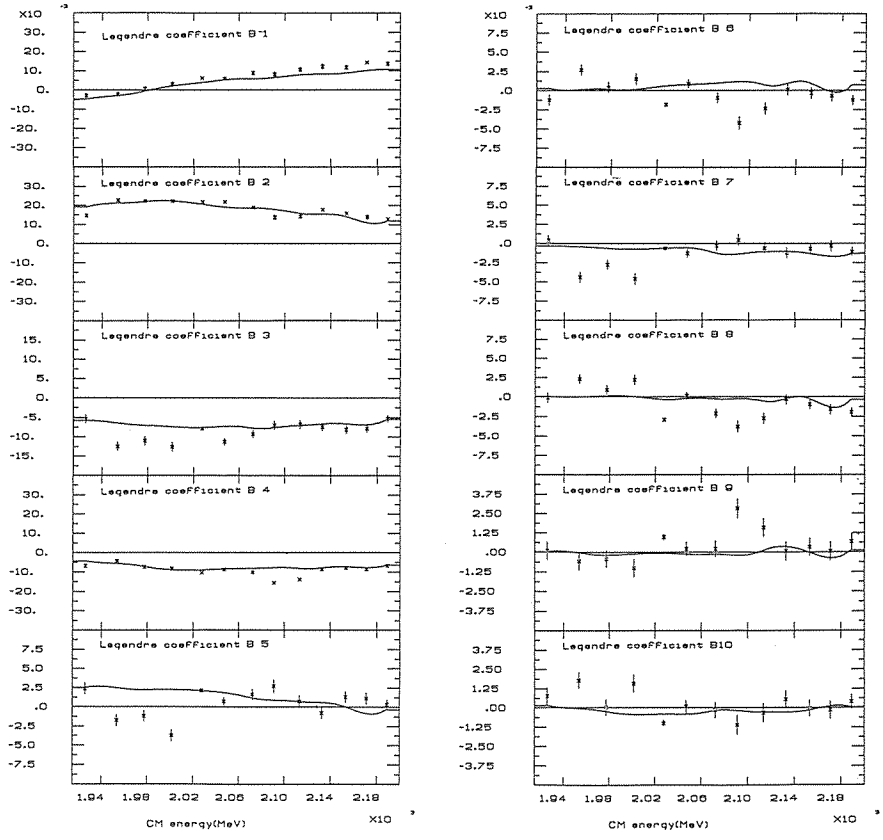

Fig. 22. Legendre coefficients B_1 to B_{10} in the present expansions as a function of E_{cm}. The solid line shows the result of the RAL partial wave analysis.

Table 8. Results of the Legendre expansion in the present

Plab MeV/c	E_{cm} MeV		B(1)	B(2)	B(3)	B(4)	B(5)
1490	1926	This exp.-	−0.28E-2	0.15E-1	−0.54E-2	−0.68E-2	0.24E-2
		RAL intp.-	−0.46E-2	0.19E-1	−0.58E-2	−0.43E-2	0.25E-2
1548	1954	This exp.-	−0.22E-2	0.23E-1	−0.12E-1	−0.43E-2	−0.18E-2
		RAL intp.-	−0.28E-2	0.21E-1	−0.64E-2	−0.57E-2	0.25E-2
1598	1977	This exp.-	0.62E-3	0.22E-1	−0.11E-1	−0.74E-2	−0.12E-2
		RAL intp.-	−0.57E-3	0.22E-1	−0.70E-2	−0.72E-2	0.22E-2
1649	2001	This exp.-	0.30E-2	0.22E-1	−0.13E-1	−0.83E-2	−0.37E-2
		RAL intp.-	0.21E-2	0.22E-1	−0.74E-2	−0.89E-2	0.23E-2
1705	2027	This exp.-	0.62E-2	0.22E-1	−0.79E-2	−0.10E-1	0.21E-2
		RAL intp.-	0.38E-2	0.21E-1	−0.76E-2	−0.89E-2	0.21E-2
1748	2047	This exp.-	0.59E-2	0.22E-1	−0.11E-1	−0.87E-2	0.71E-3
		RAL intp.-	0.52E-2	0.19E-1	−0.73E-2	−0.84E-2	0.19E-2
1803	2072	This exp.-	0.88E-2	0.19E-1	−0.92E-2	−0.10E-1	0.16E-2
		RAL intp.-	0.57E-2	0.19E-1	−0.77E-2	−0.81E-2	0.12E-2
1845	2091	This exp.-	0.81E-2	0.14E-1	−0.70E-2	−0.16E-1	0.27E-2
		RAL intp.-	0.64E-2	0.18E-1	−0.76E-2	−0.77E-2	0.88E-3
1895	2113	This exp.-	0.11E-1	0.14E-1	−0.68E-2	−0.14E-1	0.71E-3
		RAL intp.-	0.79E-2	0.16E-1	−0.70E-2	−0.81E-2	0.69E-3
1939	2133	This exp.-	0.12E-1	0.18E-1	−0.74E-2	−0.86E-2	−0.77E-3
		RAL intp.-	0.83E-2	0.15E-1	−0.66E-2	−0.78E-2	0.58E-3
1986	2153	This exp.-	0.12E-1	0.16E-1	−0.81E-2	−0.79E-2	0.13E-2
		RAL intp.-	0.88E-2	0.14E-1	−0.66E-2	−0.73E-2	0.43E-5
2027	2171	This exp.-	0.14E-1	0.14E-1	−0.78E-2	−0.86E-2	0.11E-2
		RAL intp.-	0.10E-1	0.11E-1	−0.69E-2	−0.78E-2	−0.85E-3
2069	2189	This exp.-	0.14E-1	0.13E-1	−0.53E-2	−0.69E-2	0.32E-3
		RAL intp.-	0.11E-1	0.12E-1	−0.55E-2	−0.65E-2	−0.32E-3

of the expansion was calculated as a function of the order for the highest momentum p_{in}=2069 MeV/c (E_{cm}=2189 MeV) and plotted in Fig. 21. 10th order was found to be satisfactory.

The coefficients B_n^{our} determined by the fit are plotted in Fig. 22, and listed in Table 8 together with the values of χ^2. The coefficient B_n^{RALPWA} calculated from the results of the RAL PWA are also shown by a solid line in the figure. Fig. 17 shows the polarization $\alpha_0 P_\Sigma$ calculated from our coefficients by solid curves and those from the RAL PWA by dashed curves.

Among these two sets of coefficient B_n, there are significant differences as seen in Fig. 22. The coefficients B_3, B_5 and B_7 are different each other in the E_{cm} region between 1930 and 2040 MeV, while the B_2, B_4, B_6 and B_8 are different in the E_{cm} region between 2060 and 2120 MeV.

analysis together with those of the RAL PWA (Ref. 16).

B(6)	B(7)	B(8)	B(9)	B(10)	χ^2/N_{DF}
−0.13E-2	0.38E-3	−0.12E-3	0.91E-4	0.77E-3	24.6/21
0.32E-3	−0.33E-3	0.42E-4	0.30E-4	0.16E-3	33.3/21
0.27E-2	−0.44E-2	0.23E-2	−0.57E-3	0.18E-2	19.6/20
0.14E-3	−0.44E-3	−0.12E-4	−0.35E-4	−0.72E-4	52.5/20
0.40E-3	−0.28E-2	0.88E-3	−0.43E-3	0.13E-4	18.0/20
0.18E-3	−0.64E-3	0.14E-3	−0.19E-3	−0.26E-3	34.3/20
0.15E-2	−0.46E-2	0.22E-2	−0.10E-2	0.16E-2	22.7/20
0.17E-3	−0.74E-3	0.14E-4	−0.12E-3	−0.43E-3	46.0/20
−0.18E-2	−0.63E-3	−0.29E-2	0.98E-3	−0.10E-2	25.0/20
0.60E-3	−0.62E-3	−0.33E-3	−0.79E-4	−0.41E-3	192.0/20
0.87E-3	−0.13E-2	0.14E-3	0.21E-3	0.73E-4	28.6/20
0.78E-3	−0.56E-3	−0.25E-3	−0.14E-3	−0.41E-3	72.6/20
−0.95E-3	−0.30E-3	−0.21E-2	0.22E-3	−0.15E-3	14.9/21
0.96E-3	−0.13E-2	−0.29E-3	−0.14E-3	−0.18E-3	49.3/21
−0.42E-2	0.44E-3	−0.38E-2	0.28E-2	−0.11E-2	15.2/20
0.11E-2	−0.14E-2	−0.27E-3	−0.20E-3	−0.19E-3	38.7/20
−0.23E-2	−0.60E-3	−0.28E-2	0.16E-2	−0.33E-3	18.2/20
0.70E-3	−0.11E-2	−0.56E-3	0.11E-3	−0.29E-3	51.1/20
0.90E-4	−0.12E-2	−0.33E-3	0.62E-4	0.53E-3	20.0/21
0.91E-3	−0.11E-2	−0.25E-3	0.35E-3	−0.29E-3	55.0/21
−0.37E-3	−0.69E-3	−0.95E-3	0.34E-3	−0.33E-4	18.1/21
0.88E-3	−0.13E-2	−0.29E-3	−0.28E-4	−0.15E-3	44.0/21
−0.72E-3	−0.34E-3	−0.16E-2	0.64E-4	−0.14E-3	15.4/21
−0.23E-3	−0.17E-2	−0.13E-2	−0.38E-3	0.11E-3	55.1/21
−0.13E-2	−0.11E-2	−0.20E-2	0.68E-3	0.40E-3	26.9/21
0.70E-3	−0.14E-2	−0.36E-3	0.12E-3	0.50E-4	51.5/21

4-5 Discussion on the Partial Waves

The χ^2 fits were performed to understand these characteristic features of the Legendre expansion coefficients B_n in terms of partial waves T_{jl}, where j and l denote total and orbital angular momentum, respectively. The solution of ΔReT_{jl} and ΔImT_{jl} are calculated by minimizing the χ^2 defined by

$$\chi^2=\sum_{n=1}^{10}\left[\frac{(\Delta B_n-\Delta B_n^{fit})}{\sigma_{B_n}}\right]^2, \tag{7}$$

with

$$\Delta B_n=B_n^{our}-B_n^{RALPWA}, \tag{8}$$

$$\Delta B_n^{fit}=\frac{\partial B_n}{\partial(ReT_{jl})}\,\Delta(ReT_{jl}(E_{cm}))+\frac{\partial B_n}{\partial(ImT_{jl})}\,\Delta(ImT_{jl}(E_{cm})), \tag{9}$$

where σ_{Bn}'s are the errors of B_n^{our}. In the present case, the significant partial waves which have significant contributions to the B_n's up to the B_8 are considered to be D_3, D_5, F_5, F_7, G_7, G_9, H_9 and H_{11} waves, and higher waves like the I_{11}, I_{13} and K_{13} waves are neglected.

The fits were made only at $E_{cm}=1977$ MeV and 2090 MeV, where differences were found to be large. The best solution of ΔReT_{jl}, ΔImT_{jl} and χ^2 are listed in Table 9. The values ΔB_n^{fit} obtained by the fits are plotted in Fig. 23 together with the ΔB_n. It is found from these results that no single wave can simultaneously reproduce the structures of the ΔB_n both at $E_{cm}=1977$ and 2090 MeV. However, the ΔB_n^{fit}'s for certain partial waves show close resemblances to ΔB_n's. The χ^2's of those waves are also significantly smaller than others. In particular, the D_3 and G_7 waves show such characteristics at $E_{cm}=1977$ MeV, while the F_5, H_9 and H_{11} waves at $E_{cm}=2090$ MeV.

Then, all possible combinations of (D_3, G_7) and (F_5, H_9, H_{11}) are examined at the next step. In this case, the ΔB_n^{fit} in the equation (7) are replaced by

$$\Delta B_n^{fit}=\frac{\partial B_n}{\partial(ReT_{jl})}\Delta(ReT_{jl}(E_{cm}))+\frac{\partial B_n}{\partial(ImT_{jl})}\Delta(ImT_{jl}(E_{cm}))$$
$$+\frac{\partial B_n}{\partial(ReT_{km})}\Delta(ReT_{km}(E_{cm}))+\frac{\partial B_n}{\partial(ImT_{km})}\Delta(ImT_{km}(E_{cm})), \qquad (10)$$

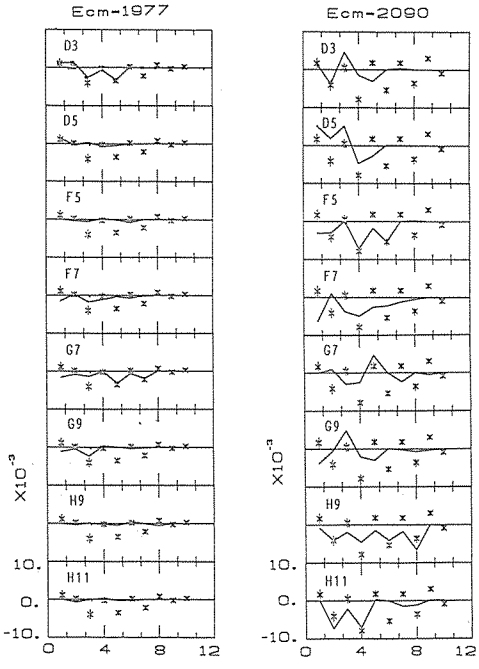

Fig. 23. Difference between the present results of B_n and that of the RAL PWA, $\Delta B_n=B_n^{our}-B_n^{RALPWA}$. The lines show the solution of the χ^2 fit to reduce this difference by changing the single partial wave amplitude of the RAL PWA.

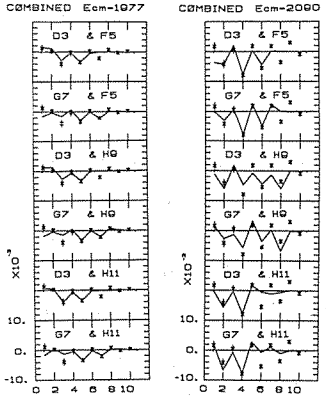

Fig. 24. Difference between the present results of B_n and that of the RAL PWA. $\Delta B_n=B_n^{our}-B_n^{RALPWA}$. The lines show the solution of the χ^2 fit to reduce the difference by changing the combination of two partial waves of the RAL PWA.

Table 9. The solution of the χ^2 fit to reduce the discrepancy between the present resuslts of Bn to those of the RAL PWA at E_{cm}=1977 MeV and E_{cm}=2090 MeV. The partial waves under test are D_3, D_5, F_5, F_7, G_7, G_9, H_9 and H_{11}. The χ^2 is defined by the equation (7).

	E_{cm}=1970			E_{cm}=2090		
wave	$Re(\Delta T_{ji})$	$Im(\Delta T_{ji})$	χ^2	$Re(\Delta T_{ji})$	$Im(\Delta T_{ji})$	χ^2
D_3	0.0203	−0.0024	20	0.0025	0.0275	281
D_5	0.0156	0.0095	51	0.0540	0.0614	197
F_5	−0.0044	0.0018	52	−0.0195	−0.0188	71
F_7	0.0200	−0.0002	46	0.0739	0.0011	182
G_7	−0.0080	−0.0070	18	−0.0267	0.0217	254
G_9	0.0015	0.0054	47	0.0236	−0.0155	271
H_9	−0.0030	0.0023	52	−0.0315	−0.0038	114
H_{11}	0.0020	−0.0008	53	0.0104	0.0171	91

where T_{jl} is one of the D_3 or G_7 waves, and T_{km} is one of the F_5, H_9 or H_{11} waves. The results of the fits are shown in Fig. 24 and are tabulated in Table 10. It is clear from these results that some improvements in terms of χ^2 is seen in all combinations, but it is

Table 10. The solution of the χ^2 fit to reduce the discrepancy between the present results of B_n to those of the RAL PWA at E_{cm}=1977 MeV and E_{cm}=2090 MeV. The combinations of partial waves under test are (D_3, F_5), (D_3, H_9), (D_3, H_{11}), (G_7, F_5), (G_7, H_9) and (G_7, H_{11}). The χ^2 is defined by the equation (7). The combination of the degree of freedom is 8.

Combination of waves	E_{cm}=1970				
	$Re(\Delta T_{ji})$	$Im(\Delta T_{ji})$	$Re(\Delta T_{km})$	$Im(\Delta T_{km})$	χ^2
D_3&G_7	0.0139	−0.0026	−0.0076	−0.0022	7.5
D_3&F_5	0.0201	−0.0021	−0.0031	0.0018	18.5
D_3&H_9	0.0201	−0.0025	−0.0004	−0.0002	19.5
D_3&H_{11}	0.0193	−0.0067	0.0042	−0.0002	15.1
G_7&F_5	−0.0097	−0.0070	0.0031	0.0021	15.4
G_7&H_9	−0.0098	−0.0074	0.0036	0.0011	14.4
G_7&H_{11}	−0.0072	−0.0101	−0.0041	0.0024	14.1

E_{cm}=2090				
$Re(\Delta T_{ji})$	$Im(\Delta T_{ji})$	$Re(\Delta T_{ji})$	$Im(\Delta T_{km})$	χ^2
0.0244	0.0438	−0.0339	0.0389	117
−0.0145	0.0013	−0.0216	−0.0195	62
−0.0130	0.0149	−0.0302	−0.0049	100
−0.0083	0.0045	0.0104	0.0172	94
0.0036	0.0125	−0.0314	−0.0154	33
0.0023	0.0145	−0.0348	−0.0038	64
0.0110	0.0052	0.0192	0.0163	75

practically impossible to single out a particular combination and to exclude others. However, it is worth noticing that the combination of G_7 and F_5 gives the smallest χ^2 among all combinations considered and reproduces the behaviour of ΔB_n very well at both energy. The physical meaning of these results will be discussed in the following section.

To make these arguments complete, the effects of the changes made in these waves upon the differential cross sections were examined. The differential cross sections were calculated from the equation (5) with the new coefficient A'_n's, which were calculated by replacing T_{jl} by $T_{jl}+\Delta T_{jl}$ for each combination. The values of χ^2 of the differential cross section measured at the RAL for these combinations and the RAL PWA are listed in Table 11. For the best combination of G_7 and F_5, the reproduced cross sections are shown in Fig. 25 together with the the original PWA predictions and the measured cross sections. It is found that the changes made here in these waves modify the differential cross sections by acceptable amounts.

Table 11. The χ^2 of the reproduced differential cross sections at $E_{cm}=1977$ MeV and $E_{cm}=12090$ MeV to the expected results at the RAL.

Combination of waves	χ^2 at $E_{cm}=1977$ MeV	χ^2 at $E_{cm}=2090$ MeV
D_3&F_5	51.31	89.66
D_3&H_9	49.90	89.03
D_3&H_{11}	58.33	96.00
G_7&F_5	67.92	103.16
G_7&H_9	64.65	96.32
G_7&H_{11}	79.97	100.32
RAL predicted	46.54	80.81
Number of data	38	39

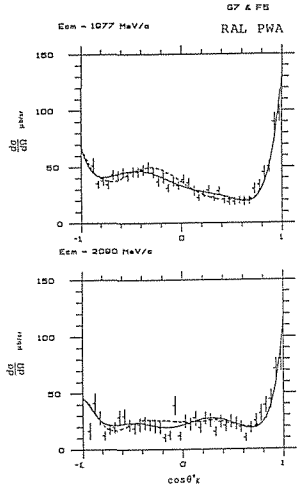

Fig. 25. Comparison of the reproduced differential cross section with the experimental results at the RAL at $E_{cm}=1977$ MeV (upper plot) and at $E_{cm}=2090$ MeV (lower plot). Solid curves are reproduced with the RAL partial waves and dashed curves are reproduced by the RAL partial waves after the F_5 and G_7 waves were modified by the present analysis.

4-6 Discussions

The polarization parameters obtained from the present experiment indicate that the D_3 and/or G_7 waves and the F_5, H_9 and/or H_{11} waves of the RAL partial wave analysis are needed to be modified to reproduce well the present results in the region around E_{cm} =1977 and 2090 MeV. Among these candidates of waves, the combination of the G_7 and F_5 waves seem to be most effective for the modification.

In these energy region, the existence of the resonance $\Delta(2000)F_{35}$ were claimed recently by D. M. Manley (Ref. 17). The CMU-LBL group claimed existence of the second resonance $\Delta(1940)D_{33}$ with marginal significance, while the K-H (Karlsruhe-Helsinki) group have found no such states in the D_3 waves (Ref. 5). This resonance is listed in the Particle Data by PDG with one star (Ref. 14). These arguments may concern the structures of the Legendre coefficients in the present results.

The peaks of ΔB_n around E_{cm}=1977 and 2090 MeV were rather sharp, so that this fact may suggest existence of some exotic states with an anomalously narrow width.

5. CONCLUSION

The polarization parameters for the $\pi^+ + p \to K^+ + \Sigma^+$ reaction have been measured with high statistics at thirteen momenta between 1490 MeV/c and 2069 MeV/c in the laboratory frame in the angular range $-0.1 \leqq \cos\theta^*_K \leqq 0.7$. In general, the present results agree well with previous data and the prediction of the RAL partial wave analysis. However, the small but systematical difference are seen at some energies. These discrepancies are found to be attributed to some structures of the Legendre coefficients of (B_3, B_5 and B_7) around E_{cm}=1977 MeV and (B_2,B_4, B_6 and B_8) around E_{cm}=2090 MeV. These results indicate the behaviors of the D_3 and/or G_7 waves and the F_5, H_9 and/or H_{11} waves must be carefully studied in datail by the partial wave analysis including the present results.

At the incident momentum of 1705 MeV/c, the polarization of the Σ^+ has been measured with the statistical errors of better than 5%, and found to be more than 0.9 in the angular range $0.1 < \cos\theta^*_K < 0.6$. These highly polarized Σ^+ were used in the measurement of the asmmetry parameter α_γ for the $\Sigma^+ \to p + \gamma$ decay, which was performed following the present experiment (Ref. 20). The large and negative value for α_γ has been confirmed with a higher accuracy than the previous measurements (Ref. 21 and 22).

Acknowledgement

The author would like to express his sincere thanks to Prof. K.Miyake, and Dr. N. Sasao for their continuous encouragement and guidance throughout this work. He is deeply grateful to Prof. T. Nakamura, Dr. R. Kikuchi, Dr. Y. Hemmi, Dr. A. Tamura, Dr. K. Imai, Dr. M. Daigo, Mr. M. Kobayashi, Mr. T. S. Nakamura, Mr. H. Kawai, Mr. M. Yoshioka, Mr. Y. Sugimoto and Mr. T. Homma for their advices and collaboration in carrying out this experiment.

Thanks are also due to the members of Cryogenics Group of KEK for their support in constructing and operating the liquid hydrogen target system.

He is indebted to the personnel at KEK, such as the members of the accelerator operation division for the stable operation of the 12 GeV/c proton synchrotron, those of the beam channel division for maintaining and tuning the K2 beam line, those of electronics division for the assistances in preparing various electronics, those of on-line group for their support in constructing and operating the on-line data taking system, those of the data handling division for their assistances in off-line analysis and those of the workshop for fabrication of the detector and the mechanical instruments.

Finally, he would like to his sincere thanks to the members of the Office of Experimental Planning and Coordination headed by Prof. A. Kusumegi and Prof. H. Hirabayashi for their proper arrangements in efficient performance of the present experiment and their hospitality.

Appendix-A Track fitting using Runge-Kutta method

In the second stage of data reduction, we calculated the first estimates of particle momentum and start point (which does not necessarily mean a "reaction point") with a spline fitting. These were used as a "starting values" of iteration in MINSQ.

MINSQ is a general program for searching parameters which minimize a sum of squares of non-linear functions. In present case, "free parameters" are five; momentum (p_x, p_y, p_z) and position (x, y at $z=0$ plane). "non-linear functions" are the difference between the expected track determined by "free parameters" and the hit position divided by the chamber resolution including the multiple Coulomb scattering. The "expected track" was generated by the Runge-Kutta method using these five free parameters tuned by MINSQ. This method was based on the Nystroem algorithm (see Handbook of National Bureau of Standards; Procedure 25,5,20) and modified by the author to vary momentum in flight according to the energy loss due to the materials of tracking devices. The spatial uncertainty due to the multiple Coulomb scattering are added to the spatial resolution of the hit position on chambers.

At every end of track generation by the Runge-Kutta method, the following quantities were calculated.

$$F_i = \frac{X^i_{measure} - X^i_{expect}}{\sqrt{\sigma^{i\ 2}_{int} + \sigma^{i\ 2}_{mul}}},$$

where σ^i_{int} is an intrinsic resolution of each chambers, σ^i_{mul} is a spatial uncertainty due to the multiple Coulomb scattering.

Then F_i's were returned to "MINSQ". In this routine, the sum of square $\sum F_i^2$ was minimized and better values for free parameters (in this case, momentum and position) ware searched from the slope of each F_i. And these new values were sent again to the Runge Kutta routine and new track was generated. Those steps were iterated till "MINSQ" would be satisfied with the result, so that the best values which gives the minumum of $\sum F_i^2$ were found.

Reference

1) de Rujula, A. H. Georgi and S. L. Glashow, Phys. Rev.**D12** (1975) 147
2) R. Koniuk and N. Isgur, Phys. Rev. **D21** (1980) 1868
3) D. J. Candlin et al., Nucl. Phys. **B226** (1983) 1
4) Yu-Li Pan et al., Nucl. Phys. **B16** (1970) 61;
   G. E. Kalmus et al., Phys. Rev. **D2** (1970) 1824;
   M. Winnik et al., Nucl. Phys. **B128** (1977) 66
5) CMU-LBL: R. Cutkosky et al., Proc. of the 1980 Toronto Conf. on Baryon Resonances, p. 19
   K-H : G.Hohler et al., Handbook of pion-nucleon scattering, Physik Daten Vol. 12-1 (1979)
6) LeCroy Research System Corp. 700 South Main Street, Spring Valey, New York 10977
7) Bouclier et al., Nucl. Instr. Meth. **149** (1970) 88
8) H. Kawai et al., Nucl. Instr. Meth. **228** (1985) 314
9) T. Tanimori et al., Nucl. Instr. Meth. **216** (1983) 57
10) M. Minowa The Memoirs of the Fuculty of Science, Kyoto University, Series A of Physics, Astrophysics, Geophysics and Chemitry **36** (1984) 109
11) R. S. Hayano et al., KEK Report 82-3 (1982);
   R. S. Hayano et al., Butsuri **37** (1982) 936
12) H. Wind, Nucl. Instr. Meth. **115** (1974) 413
13) M. J. D. Powell, Computer Journal **7** (1965) 303
14) Particle Data Group, Phys. Lett. **170B** (1986); Rev. Mod. Phys. **56** (1984)
15) Y. Oyanagi Lett. AL. Nuovo Cimento **23** (1978) 634
16) D. J. Candlin et al., Nucl. Phys. **B238** (1984) 477
17) D. M. Manley, Phys. Rev. Lett. **52** (1984) 2122
18) P. Livanos et al., Proc. of the 1980 Toronto Conf. on Baryon Resonances, p. 35
19) S. Deans et al., Nucl. Phys. **B96** (1975) 90
20) See Proceeding of the 1985 International Symposium on Lepton and Photon Interaction at High Energies. Aug. 19-24 (1985) p.350
21) L. K. Gershwin et al., Phys. Rev. **188** (1969) 2077
22) A. Mantz et al. Phys. Lett. **96B** (1980) 217